Research Square

Preprints are preliminary reports that have not undergone peer review.
They should not be considered conclusive, used to inform clinical practice,
or referenced by the media as validated information.

A new topological Cu-MOF constructed via ligand desymmetrization strategy for natural gas liquids separation

Daofeng Sun

dfsun@upc.edu.cn

China University of Petroleum (East China) https://orcid.org/0000-0003-3184-1841

Jingjing Chen

China University of Petroleum (East China)

Xiuping Liu

Linyi University

Xuemei Song

China University of Petroleum (East China)

Yinping Liu

China University of Petroleum (East China)

Fei Gao

China University of Petroleum (East China)

Xueying Feng

China University of Petroleum (East China)

Xueyan Zhang

China University of Petroleum (East China)

Yifan Zhang

China University of Petroleum (East China)

Qirong Liu

China University of Petroleum (East China)

Xiaokang Wang

China University of Petroleum (East China) https://orcid.org/0000-0003-2395-5451

Rongming Wang

China University of Petroleum (East China) https://orcid.org/0000-0002-5445-541X

Article

Keywords:

Posted Date: June 2nd, 2026

DOI: https://doi.org/10.21203/rs.3.rs-9863772/v1

License: This work is licensed under a Creative Commons Attribution 4.0 International License.
Read Full License

Additional Declarations: There is **NO** Competing Interest.

Abstract

The construction of metal-organic frameworks (MOFs) with complicated cage architectures has been proven to facilitate challenging gas separation. Herein, via ligand desymmetrization strategy, we construct a highly porous Cu-MOF, $[Cu_6(H_2O)_4(HCOO)(CPTT\text{-}NH_2)_3]$ (UPC-114, $H_4CPTT\text{-}NH_2$ = 4'-amino-5'-(4-carboxyphenyl)-[1,1':3',1"-terphenyl]-3,4",5-tricarboxylic acid). The ligand desymmetrization and amino functionalization give rise to not only the typical $Cu_2(COO)_4$ paddle-wheel, but also the tetranuclear $Cu_4(H_2O)_2(COO)_8$ cluster in UPC-114. The large cages of 26.1 Å and small cages of 13.4 Å with the shared windows of 8.8 Å surrounding with the pockets of 6.8 Å endow UPC-114 with efficient separation performance for natural gas liquids.

Introduction

Natural gas liquids (NGLs) refer to liquid hydrocarbon mixtures recovered during natural gas (methane, CH_4) extraction and processing, primarily comprising ethane (C_2H_6), propane (C_3H_8), butane (C_4H_{10}), isobutane (i-C_4H_{10}), and natural gasoline (C_5+ hydrocarbons, i.e., pentanes and heavier fractions)[1–3]. As a vital resource in the energy and chemical industries, NGLs have diverse applications. For instance, approximately 70% of ethylene production feedstocks originate from C_2H_6 derived from NGLs, with ethylene serving as a fundamental building block for polymers such as polyethylene, polyvinyl chloride, and other organic chemicals[4–6]. C_3H_8 is not only widely utilized as liquefied petroleum gas (LPG) for domestic and commercial purposes, including residential heating and automotive fuel, but also acts as a key feedstock for ethylene and propylene production—propylene being the primary component of polypropylene-based materials[7–9]. C_4H_{10} can be converted via isomerization to produce i-C_4H_{10}, which is subsequently used in alkylation processes to generate alkylates as high-octane gasoline additives[10–12]. As a result, the purification of NGLs is of considerable significance to the petroleum industry and presents substantial economic incentives for natural gas producers, thereby driving industrial research to develop alternative gas separation technologies.

The industrial separation of NGLs is conventionally achieved through cold residue recycle process and gas subcooled process[13]. In these techniques, the gas stream is initially cooled to extremely low temperatures via heat exchange utilizing overhead streams, side reboilers, and/or external refrigerants, followed by a depressurization step that induces rapid expansion and further cooling, thereby facilitating the condensation of C_2H_6, C_3H_8, and heavier hydrocarbons[14]. However, these processes must be conducted under rigorously controlled cryogenic conditions, resulting in substantial energy consumption. In contrast, non-thermal-driven adsorptive separation technology operates on the basis of chemical affinity or molecular size rather than differences in boiling or condensation points[15–17]. Consequently, such separations can be performed under mild conditions, significantly reducing both operational costs and energy input. Adsorbents constitute the core of adsorption technology, as the adsorption performance (adsorption capacity and selectivity) fundamentally dictates the efficiency of

the separation process. Therefore, the development of effective adsorbents to enable more energy-efficient purification of NGLs is of paramount importance.

Metal-organic frameworks (MOFs) are a class of emerging crystalline porous materials constructed through self-assembly of inorganic metal nodes and organic ligands, forming periodic network structures[18–20]. Owing to their tunable pore sizes/shapes and modifiable pore surfaces, MOFs have demonstrated considerable application potential across diverse fields, particularly in gas adsorption and separation[21–23]. Over the past decades, numerous studies have reported the use of MOFs for gas separation, revealing several design strategies, such as interpenetration, Lewis basic sites (LBSs)[24], open metal sites (OMSs)[25], and pore space partition[26]. For instance, Liu et al. successively developed the JLU-Liu series materials employing a ternary secondary building unit (SBU)-based synthetic strategy[27]. Among them, JLU-Liu15 exhibited the best C_3H_8/CH_4 separation performance, achieving a high selectivity of 461.5. Zhai et al. proposed a dual-nanotrap construction strategy, wherein the spatial arrangement of ligands generates two types of complementary aromatic ring-confined nanotraps within the framework[28]. By leveraging the synergistic effects of selective nanotraps via multiple C–H···π interactions and molecular size sieving, this approach enhances thermodynamic differences and mitigates competitive adsorption, thereby enabling highly efficient adsorptive separation of C_2H_6 and C_3H_8. Zhang et al. reported the ultramicroporous NKMOF-15 with pore sizes of approximately 5.7 Å × 5.3 Å[29]. Through precise control over pore size and the introduction of O/N atoms on the pore surface, NKMOF-15 exhibits enhanced adsorption affinity for C_2H_6 and C_3H_8 via hydrogen bonding and C–H···π interactions. However, reports on MOFs specifically designed for the separation of $C_2H_6/C_3H_8/C_4H_{10}$ remain almost blank.

Herein, we constructed a three-dimensional (3D) microporous Cu-MOF, $[Cu_6(H_2O)_4(HCOO)(CPTT\text{-}NH_2)_3]$ (UPC-114, $H_4CPTT\text{-}NH_2$ = 4'-amino-5'-(4-carboxyphenyl)-[1,1':3',1"-terphenyl]-3,4",5-tricarboxylic acid), via ligand desymmetrization strategy (Fig. 1). The ligand desymmetrization and amino functionalization afford two different SBUs, including the typical $Cu_2(COO)_4$ paddle-wheel and tetranuclear $Cu_4(H_2O)_2(COO)_8$ cluster. The large cages with an inner diameter of 26.1 Å and the small cages with an inner diameter of 13.4 Å sharing the window of 8.8 Å and surrounding with pockets of 6.8 Å provide a foundation for the efficient separation of $C_2H_6/C_3H_8/C_4H_{10}$, as corroborated by adsorption isotherms, dynamic breakthrough curves, grand canonical Monte Carlo (GCMC) simulations, and density functional theory (DFT) calculations.

Results

Structure design and characterization of UPC-114

The synthetic procedure of $H_4CPTT\text{-}NH_2$ was detailed in the supporting information. Bright green block crystals of UPC-114 with high crystallinity were afforded by the solvothermal reaction of $Cu(NO_3)_2$ and

H_4CPTT-NH_2. Single-crystal X-ray diffraction (SCXRD) analysis revealed that UPC-114 crystallized in the tetragonal *I4/mmm* space group. The asymmetric unit consists of four Cu atoms with a half of occupancy, four Cu atoms with a quarter of occupancy, two H_2O molecules with a half of occupancy, four H_2O molecules with a quarter of occupancy, half of a formic acid, and one and a half of deprotonated H_4CPTT-NH_2 (Fig. S2). Cu1-Cu4 atoms adopt the square pyramidal geometry to connect with four carboxylic O atoms and one H_2O molecule, forming the typical binuclear $Cu_2(COO)_4$ paddle-wheel (Fig. 2a, S3a). Cu5 and Cu6 also form paddle-wheel SBU and the coordination of formic acid on Cu5 links the adjacent two paddle-wheels (Fig. S3a). Cu7 adopts the distorted octahedral geometry to connect with four carboxylic O atoms and two μ_3-H_2O molecules, whereas Cu8 adopts the square pyramidal geometry to connect with four carboxylic O atoms and one μ_3-H_2O molecule, thus forming the tetranuclear $Cu_4(H_2O)_2(COO)_8$ cluster (Fig. 2a, S3a). Each H_4CPTT-NH_2 ligand links either three binuclear SBUs and one tetranuclear SBU or two binuclear SBUs and two tetranuclear SBUs (Fig. 2a, S3b), producing 3D structure with two kinds of cages sharing the window of 8.8 Å and surrounding with pockets of 6.8 Å (Fig. 2b, S4). The inner diameters of the cages are 26.1 and 13.4 Å, respectively (Fig. S5-6). The structure can be simplified as a new 4,4,4,4,5,8-c *cjj* topology with point symbol of $\{4^{12}.6^4.8^{12}\}\{4^2.5^4.6^2.8^2\}\{4^2.5^4\}\{4^2.6^3.7\}_4\{4^2.6^4\}_2\{4^6\}_2$ according to TOPOS Pro (Fig. 2c-d). The solvent-accessible porosity of UPC-114 is calculated as 77.5%, and the theoretical pore volume is 1.46 cm^3/g based on Platon calculations[30].

Powder X-ray diffraction (PXRD) patterns demonstrated the excellent phase purity of as-synthesized UPC-114 (Fig. S7). Thermogravimetric (TG) analysis revealed an initial weight loss before 100°C, corresponding to the release of solvents, followed by framework stability up to approximately 300°C (Fig. S8). The disappearance of characteristic absorption peaks in the range of 1750 – 1650 cm^{-1} on the infrared (IR) spectrum of UPC-114 indicated the deprotonation of carboxyl groups (Fig. S9).

Permanent porosity and gas adsorption

The permanent porosity of UPC-114 was proved by the reversible type I nitrogen (N_2) isotherms at 77 K with a maximum adsorption capacity of 830.75 cm^3/g (Fig. 3a). The calculated Brunauer-Emmett-Teller (BET) surface area reached 2538.95 m^2/g, with a high pore volume of 1.28 cm^3/g. The pore size distribution analyzed with non-local DFT revealed the primary peaks centered at 12.6 and 25.1 Å. The experimental porosity of UPC-114 closely matched the theoretical value calculated from the crystal structure, demonstrating the complete and effective activation. The ultrahigh porosity and specific surface area prompted the further evaluation of UPC-114 for the separation of NGLs. Single-component adsorption/desorption isotherms of UPC-114 for C_2H_6, C_3H_8, and C_4H_{10} were obtained at 273 and 298 K. As expected, the adsorption capacity followed the order of $C_4H_{10} > C_3H_8 > C_2H_6$. At 273 K, the adsorption capacities of C_2H_6, C_3H_8, and C_4H_{10} were 101.28 cm^3/g (4.52 mmol/g), 254.60 cm^3/g (11.36 mmol/g), and 266.83 cm^3/g (11.91 mmol/g), respectively (Fig. 3b), and the adsorption uptakes at 298 K reached

71.45 cm^3/g (3.19 mmol/g), 167.57 cm^3/g (7.48 mmol/g), and 242.62 cm^3/g (10.83 mmol/g) for C_2H_6, C_3H_8, and C_4H_{10}, respectively (Fig. 3c). The above results indicated the optimal pore confinement and effective binding interactions of UPC-114 for C_4H_{10}. It is worth noting that the superior C_4H_{10} uptake of UPC-114 is comparable with many reported benchmark porous adsorbents (Fig. 3d), such as JUC-644 (10.45 mmol/g)[31], Y-ftw-MOF-2 (11.19 mmol/g)[32], and LIFM-233 (11.73 mmol/g)[33].

The Virial equation was employed to calculate the adsorption enthalpy (Q_{st}), providing a quantitative measure of the affinity between UPC-114 and gas molecules (Fig. S10-12). The Q_{st} value of C_4H_{10} (30.62 kJ/mol) at near zero coverage is higher than those of C_2H_6 (17.52 kJ/mol) and C_3H_8 (29.19 kJ/mol), indicating the stronger affinity of UPC-114 for C_4H_{10} (Fig. 3e). Notably, the moderate C_4H_{10} Q_{st} of UPC-114 is lower than those of many C_4H_{10}-selective adsorbents, such as LIFM-Z1 (39.3 kJ/mol)[34], MAF-68 (40.4 kJ/mol)[35], and ZJU-HOF-8a (41.3 kJ/mol)[36], suggesting the facile regeneration of UPC-114 with lower energy cost. To predict the separation potential of UPC-114 for equimolar C_3H_8/C_2H_6 and C_4H_{10}/C_2H_6 mixture, ideal adsorbed solution theory (IAST) was used to calculate the selectivity (Fig. S13-18). At 273 K and 1 bar, the selectivity of UPC-114 for C_3H_8/C_2H_6 and C_4H_{10}/C_2H_6 reached 5.81 and 31.65, respectively, whereas the selectivity of C_3H_8/C_2H_6 and C_4H_{10}/C_2H_6 at 298 K decreased to 4.06 and 20.03, respectively (Fig. 3f). Abundant OMSs, complicated cage architectures, superior C_4H_{10} uptake, moderate Q_{st} value, and appreciable selectivity make UPC-114 a potential candidate for $C_2H_6/C_3H_8/C_4H_{10}$ separation (Table S2).

Dynamic breakthrough experiments

The dynamic breakthrough experiments were subsequently conducted at 298 K and 1 bar to validate the practical separation performance. The activated samples of UPC-114 were packed in a quartz column, and binary equimolar gas mixture passed through the column with a total flow rate of 2 mL/min to achieve effective separation. For C_3H_8/C_2H_6 (50/50, v/v) mixture, the signal of C_2H_6 was first detected at 26.2 min/g, and C_3H_8 broke through after adsorption saturation at 72.1 min/g (Fig. 4a). The dynamic adsorption capacity of C_3H_8 was 75.81 cm^3/g, which is higher than that of C_2H_6 (13.88 cm^3/g), and the separation factor reached 5.46 (Fig. S19) with a C_2H_6 productivity of 2.90 mmol/g (Fig. S20). For C_4H_{10}/C_2H_6 (50/50, v/v) mixture, the signals of C_2H_6 and C_4H_{10} were detected at 27.8 min/g and 169.4 min/g, respectively (Fig. 4b). The dynamic adsorption capacities of C_4H_{10} and C_2H_6 were 176.90 cm^3/g and 14.50 cm^3/g, respectively, with a separation factor of 12.19 (Fig. S21) and a C_2H_6 productivity of 8.59 mmol/g (Fig. S22). The considerable breakthrough interval time and separation factor suggested the efficient C_3H_8/C_2H_6 and C_4H_{10}/C_2H_6 separation.

To further validate the practical applicability for the separation of NGLs, breakthrough experiment of $C_4H_{10}/C_3H_8/C_2H_6$ (20/34/46, v/v/v) ternary mixture (5 mL/min) was conducted on UPC-114. The effective separation was achieved with C_2H_6, C_3H_8, and C_4H_{10} sequentially breaking through at 20.0

min/g, 53.5 min/g, and 172.6 min/g, respectively (Fig. 4c). The calculated pure C_2H_6 productivity reached 5.37 mmol/g (Fig. S23). This superior separation performance of UPC-114 for NGLs persisted at different flow rates (Fig. 4d), at different temperatures (Fig. 4e), and under humid conditions (Fig. S24). In addition, the efficient $C_4H_{10}/C_3H_8/C_2H_6$ separation performance was retained over three consecutive cycles (Fig. 4f), proving its excellent cycling stability, which is a key metric for practical application. The excellent stability of UPC-114 was subsequently proved by the unchanged crystallinity and porosity, as evidenced by the PXRD patterns (Fig. S7) and N_2 adsorption isotherms (Fig. S25) after breakthrough tests.

Theoretical calculation

To elucidate the distinct adsorption behavior of C_2H_6, C_3H_8, and C_4H_{10} in UPC-114, theoretical calculation was performed to probe the preferential adsorption sites and host-guest interactions. According to GCMC simulations on the density distribution of C_2H_6, C_3H_8, and C_4H_{10} in UPC-114 at 298 K and 1 bar, the main adsorption sites are located near the paddle-wheels, tetranuclear clusters, and aromatic frameworks modified with amino groups, with density order of $C_4H_{10} > C_3H_8 > C_2H_6$ (Fig. 5a-c). The optimal adsorption sites and binding energies of C_2H_6, C_3H_8, and C_4H_{10} in UPC-114 were subsequently obtained with dispersion-corrected DFT calculations. The adsorption sites derived from DFT calculations were in good agreement with GCMC simulation results. Attributed to the largest molecular dimensions, C_4H_{10} exhibits the highest adsorption energy (61.46 kJ/mol), which enables simultaneous interactions with the paddle-wheels and tetranuclear clusters, as well as the formation of C–H···O and C–H···N hydrogen bonds with carboxyl and amino groups (Fig. 5d). C_3H_8, with intermediate molecular size, displays interaction sites analogous to those of C_4H_{10} (Fig. 5e), albeit with a lower adsorption energy (40.41 kJ/mol). C_2H_6, predominantly confined within the pockets, forms weak C–H···O hydrogen bonds with the framework (Fig. 5f), corresponding to the lowest adsorption energy (31.32 kJ/mol).

Discussion

In summary, via ligand desymmetrization strategy, we designed and synthesized UPC-114 based on $Cu_2(COO)_4$ paddle-wheel, tetranuclear $Cu_4(H_2O)_2(COO)_8$ cluster, and amino-functionalized tetracarboxylic H_4CPTT-NH_2 ligand. Notably, UPC-114 exhibits a new *cjj* topology and demonstrates ultrahigh adsorption capacity for C_4H_{10} (10.83 mmol/g) at 298 K, surpassing the performance of most known porous materials. Breakthrough tests proved the efficient C_3H_8/C_2H_6, C_4H_{10}/C_2H_6, and $C_4H_{10}/C_3H_8/C_2H_6$ separation on UPC-114, highlighting its potential for the separation of NGLs. This work provides a blueprint to the design of intricate MOF architectures via ligand desymmetrization strategy, targeting the separation of gas mixture with complex components.

Methods

Materials and instruments

All reagents were commercially available and used without further purification. ^{1}H nuclear magnetic resonance (NMR) spectrum was obtained on a Bruker 400 MHz nuclear magnetic resonance spectrometer. Single crystal X-ray diffraction experiment was carried out on a SuperNova diffractometer equipped with mirror Cu-Kα radiation (λ = 1.54184 Å) and an Eos CCD detector. PXRD patterns were collected on a Bruker D8-Focus Bragg-Brentano X-ray powder diffractometer equipped with a Cu sealed tube at 40 kV and 15 mA. TGA test was performed on a Mettler Toledo TGA/DSC1 instrument under a static N_2 atmosphere with a heating rate of 10°C/min at the range of 40–900°C. IR spectrum was collected on a Nicolet 330 FTIR Spectrometer within 4000 – 400 cm^{-1} region. Gas sorption measurements were conducted on a Micrometritics ASAP 2020 surface area analyzer. Breakthrough experiments were carried out on BSD-MAB multi-component adsorption breakthrough curve analyzer monitored by Hiden HPR-20EGA mass spectrometer.

Synthesis of UPC-114

A mixture of H_4CPTT-NH_2 ligand (5 mg, 0.01 mmol), $Cu(NO_3)_2{\cdot}3H_2O$ (12 mg, 0.05 mmol), and HBF_4 (70 μL) in 2 mL of N,N'-dimethylformamide (DMF) and 0.5 mL of H_2O was ultrasonically dissolved in a Pyrex vial (10 mL) and heated at 90°C for 18 h. The vial was then cooled to room temperature at a rate of 5°C/h. The obtained bright green block crystals were filtered, washed with methanol and dried in air (yield: 78%).

X-ray data collection and structure determination of UPC-114

The as-synthesized crystals were taken from the mother liquid without further treatment, transferred to oil and mounted on to a loop for single crystal X-ray data collection. The data were collected on an Agilent Technologies SuperNova diffractometer equipped with graphite monochromatic Cu Kα radiation (λ = 1.54184 Å). With the help of Olex2, the structure was solved with the Superflip structure solution program using charge flipping and refined with the ShelXL refinement package using least squares minimization. The structure was treated anisotropically, whereas the hydrogen atoms were placed in calculated ideal positions and refined as riding on their respective nonhydrogen atoms. PLATON and SQUEEZE were used to calculate the diffraction contribution of the solvent molecules and thereby produced a set of partly solvent-free diffraction intensities.

Data availability

The data supporting this study are provided in the Supplementary Information. Additional data are available from the corresponding author upon request. The X-ray crystallographic coordinates for structure reported in this Article have been deposited at the Cambridge Crystallographic Data Centre (CCDC), under deposition number 2530133. These data can be obtained free of charge from The Cambridge Crystallographic Data Centre via www.ccdc.cam.ac.uk/data_request/cif.

Declarations

Competing interests

The authors declare no competing interests.

Author contributions

Jingjing Chen: Investigation, Methodology, Writing - original draft, Conceptualization, Visualization. Xiuping Liu: Software, Validation, Investigation. Xuemei Song: Investigation, Validation. Yinping Liu: Investigation, Formal analysis. Fei Gao: Investigation, Data curation. Xueying Feng: Investigation, Validation. Xueyan Zhang: Investigation, Validation. Yifan Zhang: Validation, Formal analysis. Qirong Liu: Validation, Formal analysis. Xiaokang Wang: Writing - original draft, Data curation, Conceptualization, Visualization. Rongming Wang: Writing - review & editing, Resources, Funding acquisition, Supervision. Daofeng Sun: Writing - review & editing, Supervision, Resources, Project administration, Funding acquisition, Methodology. All authors discussed the results and commented on the manuscript.

Acknowledgments

This work was supported by the National Natural Science Foundation of China (22005340), the Qingdao Natural Science Foundation (24-4-4-zrjj-179-jch), and the Natural Science Foundation of Shandong Province (ZR2025MS150).

References

1. Ghosh K, Salas SD, Garciadiego A, Dunn JB, Dowling AW. Multiscale Equation-Oriented Optimization Decreases the Carbon Intensity of Shale Gas to Liquid Fuel Processes. *ACS Sustainable Chem Eng* **12**, 10351-10362 (2024).
2. Kazemi A. Natural gas liquids (NGL) recovery: A framework for environmental, technical and economic assessments and optimizations. *Chem Eng Sci* **316**, 121928 (2025).
3. Qyyum MA, Naquash A, Haider J, Al-Sobhi SA, Lee M. State-of-the-art assessment of natural gas liquids recovery processes: Techno-economic evaluation, policy implications, open issues, and the way forward. *Energy* **238**, 121684 (2022).

4. Amghizar I, Vandewalle LA, Van Geem KM, Marin GB. New Trends in Olefin Production. *Engineering* **3**, 171-178 (2017).
5. Wang Z*, et al.* Kilogram-Scale Fabrication of a Robust Olefin-Linked Covalent Organic Framework for Separating Ethylene from a Ternary C_2 Hydrocarbon Mixture. *J Am Chem Soc* **145**, 21483-21490 (2023).
6. Jiang X*, et al.* Integration of ordered porous materials for targeted three-component gas separation. *Nat Commun* **16**, 694 (2025).
7. Christopher CCE, Dutta A, Farooq S, Karimi IA. Process Synthesis and Optimization of Propylene/Propane Separation Using Vapor Recompression and Self-Heat Recuperation. *Ind Eng Chem Res* **56**, 14557-14564 (2017).
8. Wang Y-B*, et al.* A Microporous Hydrogen-Bonded Organic Framework with Alkynyl Sites for Highly Efficient Propane/Propylene Separation. *J Am Chem Soc* **147**, 24403-24412 (2025).
9. Zhang P*, et al.* One-step propylene purification from a quaternary mixture by a single physisorbent. *Nat Commun* **16**, 11316 (2025).
10. Velázquez HD*, et al.* Recent progress on catalyst technologies for high quality gasoline production. *Catal Rev* **65**, 1079-1299 (2022).
11. Liu Y*, et al.* Room-Temperature Synthesis of Zeolite Membranes toward Optimized Microstructure and Enhanced Butane Isomer Separation Performance. *J Am Chem Soc* **145**, 7718-7723 (2023).
12. Peng Y*, et al.* Interaction-selective molecular sieving adsorbent for direct separation of ethylene from senary C_2-C_4 olefin/paraffin mixture. *Nat Commun* **15**, 625 (2024).
13. Islam M, Al-Sobhi SA, Naquash A, Qyyum MA, Lee M. Optimal process selection for natural gas liquids recovery: Energy, exergy, economic, and environmental perspectives. *Energy* **289**, 129757 (2024).
14. Usman M, Pervaiz E. An Inclusive Review on the Assessment of Different Techniques for Natural Gas Liquid Recovery. *Chem Eng Technol* **46**, 1397-1410 (2023).
15. Yue B, Liu S, Chai Y, Wu G, Guan N, Li L. Zeolites for separation: Fundamental and application. *J Energy Chem* **71**, 288-303 (2022).
16. Zhao Y-L, Zhang X, Li M-Z, Li J-R. Non-CO_2 greenhouse gas separation using advanced porous materials. *Chem Soc Rev* **53**, 2056-2098 (2024).
17. Paz L, Gentil S, Fierro V, Celzard A. Activated carbons outperform other sorbents for biogas desulfurization. *Chem Eng J* **506**, 160304 (2025).
18. Sun N, Shah SSA, Lin Z, Zheng Y-Z, Jiao L, Jiang H-L. MOF-Based Electrocatalysts: An Overview from the Perspective of Structural Design. *Chem Rev* **125**, 2703-2792 (2025).
19. Ye Z, Jiang Y, Li L, Wu F, Chen R. Rational Design of MOF-Based Materials for Next-Generation Rechargeable Batteries. *Nano-Micro Lett* **13**, 203 (2021).
20. Chai L, Pan J, Hu Y, Qian J, Hong M. Rational Design and Growth of MOF-on-MOF Heterostructures. *Small* **17**, 2100607 (2021).

21. Li X, Chen K, Guo R, Wei Z. Ionic Liquids Functionalized MOFs for Adsorption. *Chem Rev* **123**, 10432-10467 (2023).
22. Wang X*, et al.* Metal-organic frameworks for C_2H_2/CO_2 separation: Recent development. *Coord Chem Rev* **482**, 215093 (2023).
23. Zhang Y*, et al.* MOF membranes for gas separations. *Prog Mater Sci* **151**, 101432 (2025).
24. Gu X-W*, et al.* Immobilization of Lewis Basic Sites into a Stable Ethane-Selective MOF Enabling One-Step Separation of Ethylene from a Ternary Mixture. *J Am Chem Soc* **144**, 2614-2623 (2022).
25. Zeng H*, et al.* Induced Fit of C_2H_2 in a Flexible MOF Through Cooperative Action of Open Metal Sites. *Angew Chem Int Ed* **58**, 8515-8519 (2019).
26. Chen Y*, et al.* Multi-Stage Optimization of Pore Size and Shape in Pore-Space-Partitioned Metal-Organic Frameworks for Highly Selective and Sensitive Benzene Capture. *Angew Chem Int Ed* **64**, e202415576 (2024).
27. Luo X*, et al.* Three Metal–Organic Frameworks Based on Binodal Inorganic Building Units and Hetero-O, N Donor Ligand: Solvothermal Syntheses, Structures, and Gas Sorption Properties. *Cryst Growth Des* **15**, 4901-4907 (2015).
28. Li S-Y*, et al.* Metal–organic frameworks with two different-sized aromatic ring-confined nanotraps for benchmark natural gas upgrade. *Chem Sci* **15**, 17547-17555 (2024).
29. Wang T*, et al.* Fabricating a Robust Ultramicroporous Metal-Organic Framework for Purifying Natural Gas and Coal Mine Methane. *Small* **20**, 2407701 (2024).
30. Spek AL. PLATON SQUEEZE: A Tool for the Calculation of the Disordered Solvent Contribution to the Calculated Structure Factors. *Acta Crystallog C* **71**, 9-18 (2015).
31. Chang J*, et al.* Synthesis of three-dimensional covalent organic frameworks through a symmetry reduction strategy. *Nat Chem* **17**, 571-581 (2025).
32. Luebke R*, et al.* Versatile rare earth hexanuclear clusters for the design and synthesis of highly-connectedftw-MOFs. *Chem Sci* **6**, 4095-4102 (2015).
33. Meng L-L*, et al.* Introducing π-electron-rich aromatic rings into a robust Zr-MOF for efficient natural gas purification and C_3H_8/n-C_4H_{10} recovery. *J Mater Chem A* **12**, 13689-13693 (2024).
34. Zheng H-T*, et al.* Three-dimensional linker-promoted hierarchical porous metal–organic framework for natural gas purification. *Sep Purif Technol* **354**, 129466 (2025).
35. Li Y-G*, et al.* Selective adsorption of C_{2+} alkanes over methane by using a zinc tris-pyrazolate framework. *J Mater Chem A* **13**, 38034-38038 (2025).
36. Jiang C*, et al.* Supramolecular Entanglement in a Hydrogen-Bonded Organic Framework Enables Flexible-Robust Porosity for Highly Efficient Purification of Natural Gas. *Angew Chem Int Ed* **63**, e202404734 (2024).

Figures

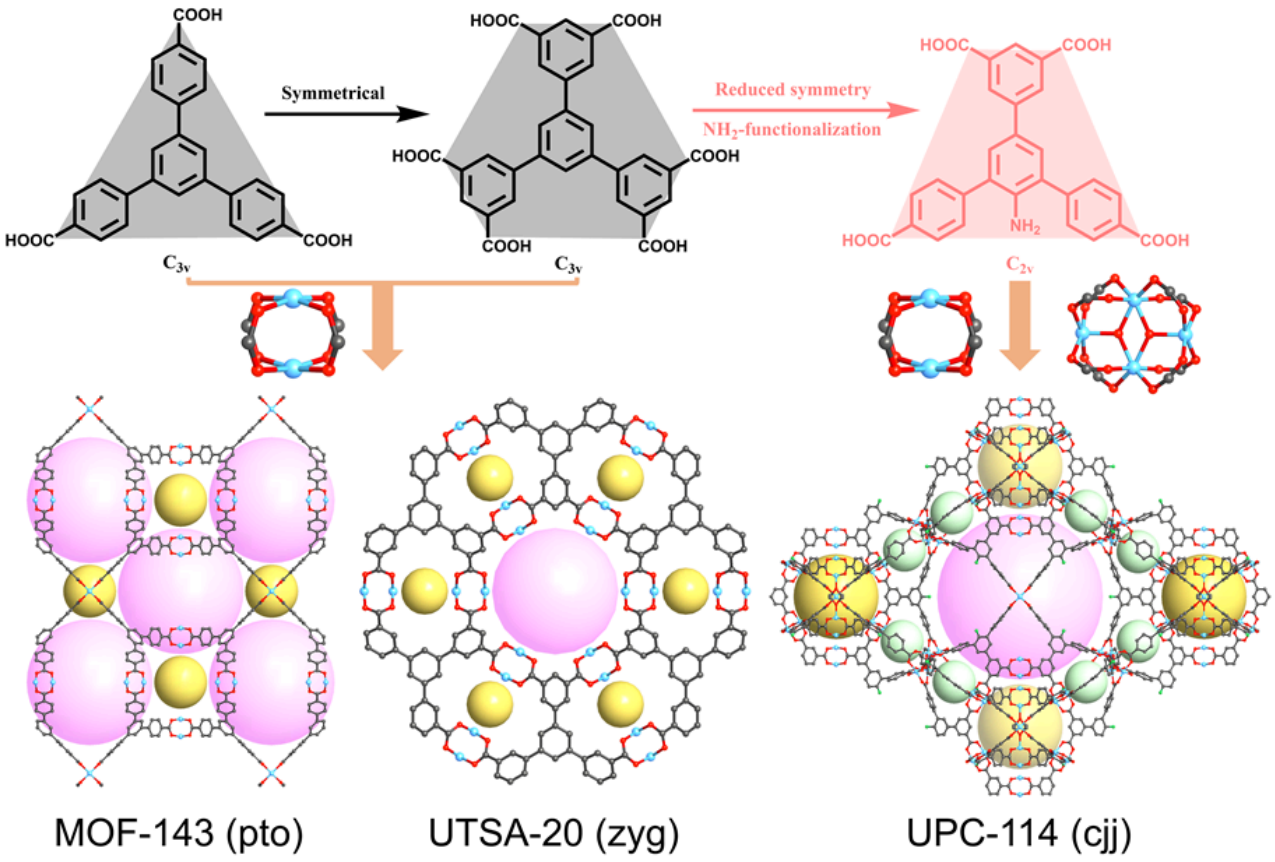


Figure 1

Illustration of UPC-114 constructed via ligand desymmetrization strategy. Including the process of ligand desymmetrization, and corresponding structures with different topologies.

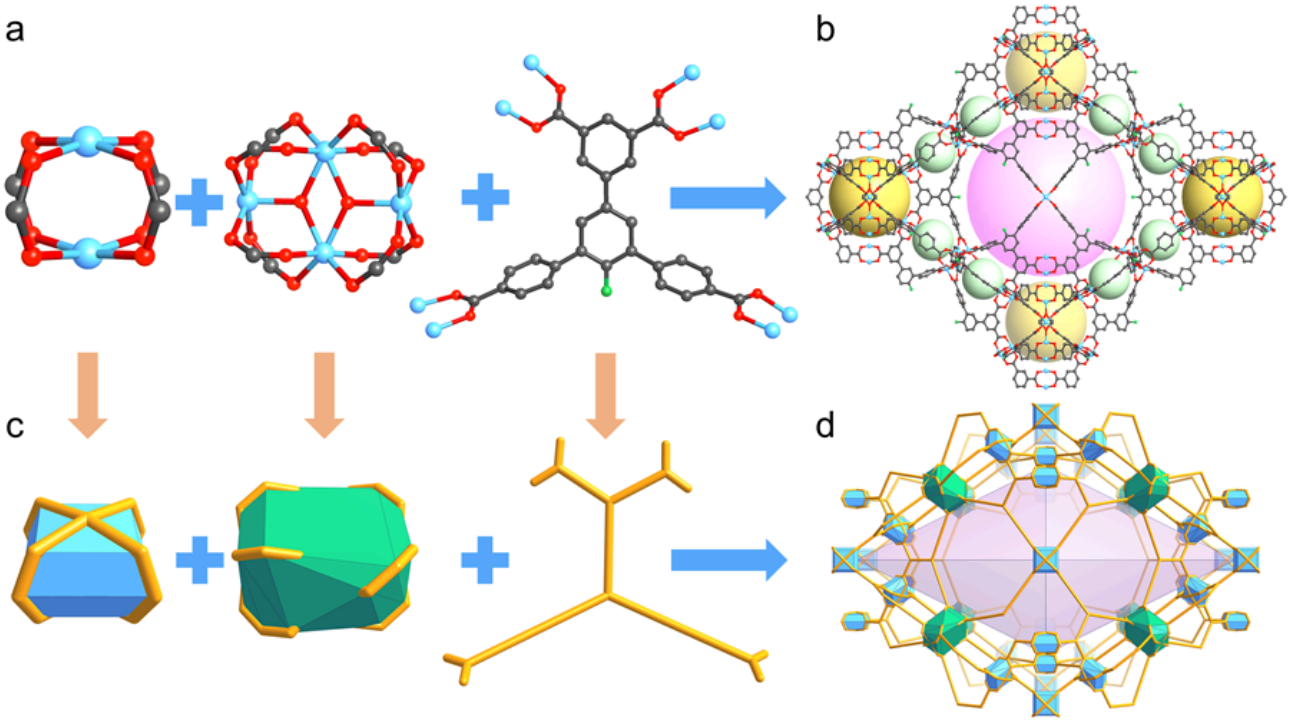


Figure 2

Structure of UPC-114. a Coordination modes of Cu and H_4CPTT-NH_2 in UPC-114. **b** 3D structure of UPC-114 with two kinds of cages surrounding with pockets. Cu, blue; C, gray; N, green; O, red. H atoms are omitted for clarity. **c** Simplified geometries of metal clusters and ligand. **d** Simplified *cjj* topology of UPC-114.

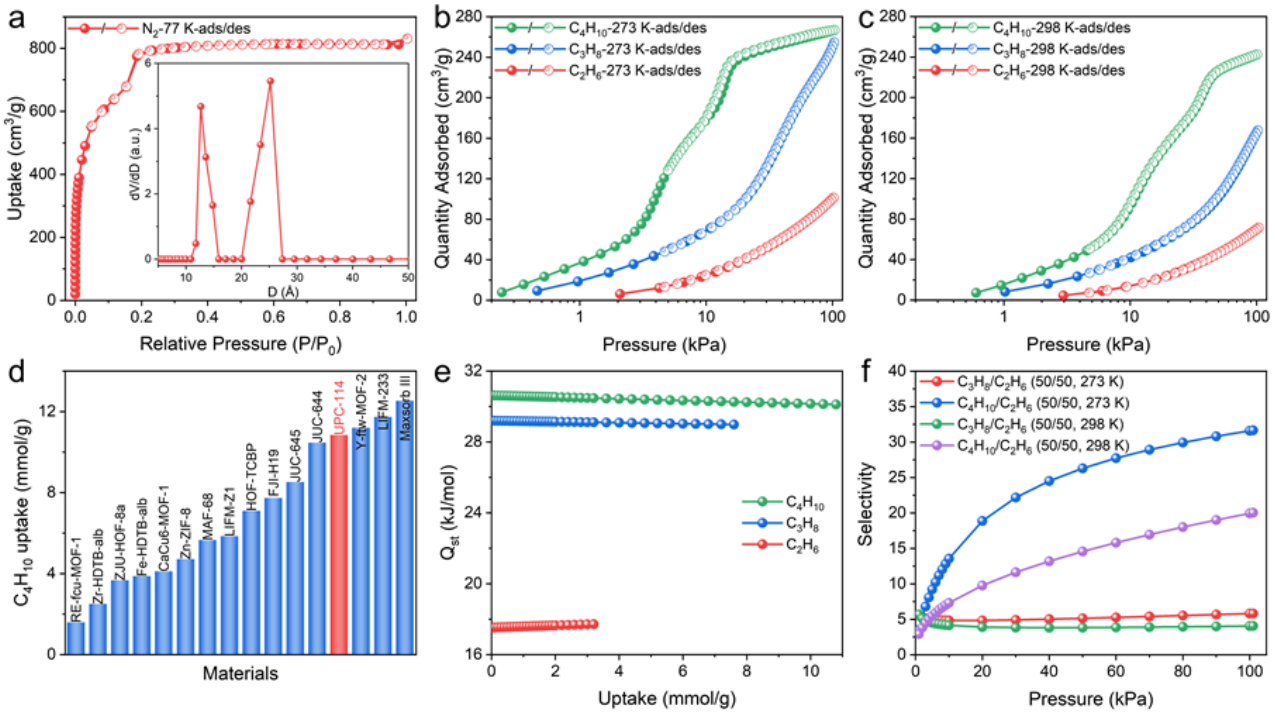


Figure 3

Gas adsorption performance of UPC-114. **a** N_2 adsorption/desorption isotherms and pore size distribution of UPC-114 at 77 K. Single-component adsorption/desorption isotherms of UPC-114 for C_2H_6, C_3H_8, and C_4H_{10} at **b** 273 K and **c** 298 K. **d** Comparison of C_4H_{10} uptake of representative materials at 298 K and 1 bar. **e** Adsorption enthalpy of UPC-114 for C_2H_6, C_3H_8, and C_4H_{10}. **f** IAST selectivity of UPC-114 for equimolar C_3H_8/C_2H_6 and C_4H_{10}/C_2H_6 mixture at 273 K and 298 K.

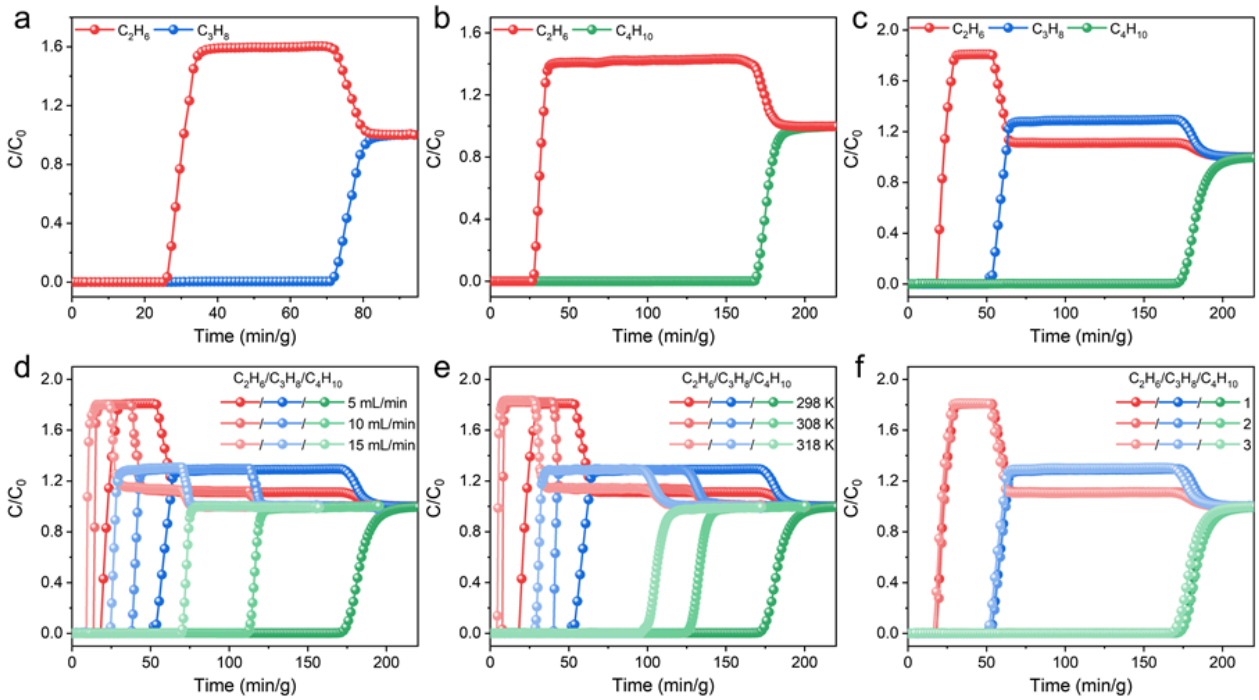


Figure 4

Dynamic breakthrough experiments of UPC-114. Breakthrough curves of **a** C_3H_8/C_2H_6 (50/50, v/v) binary mixture (2 mL/min), **b** C_4H_{10}/C_2H_6 (50/50, v/v) binary mixture (2 mL/min), and **c** $C_4H_{10}/C_3H_8/C_2H_6$ (20/34/46, v/v/v) ternary mixture (5 mL/min) on UPC-114 at 298 K and 1 bar. **d** Breakthrough curves of $C_4H_{10}/C_3H_8/C_2H_6$ (20/34/46, v/v/v) ternary mixture at different flow rates on UPC-114 at 298 K and 1 bar. **e** Breakthrough curves of $C_4H_{10}/C_3H_8/C_2H_6$ (20/34/46, v/v/v) ternary mixture (5 mL/min) on UPC-114 at different temperatures and 1 bar. **f** Cycling breakthrough curves of $C_4H_{10}/C_3H_8/C_2H_6$ (20/34/46, v/v/v) ternary mixture (5 mL/min) on UPC-114 at 298 K and 1 bar.

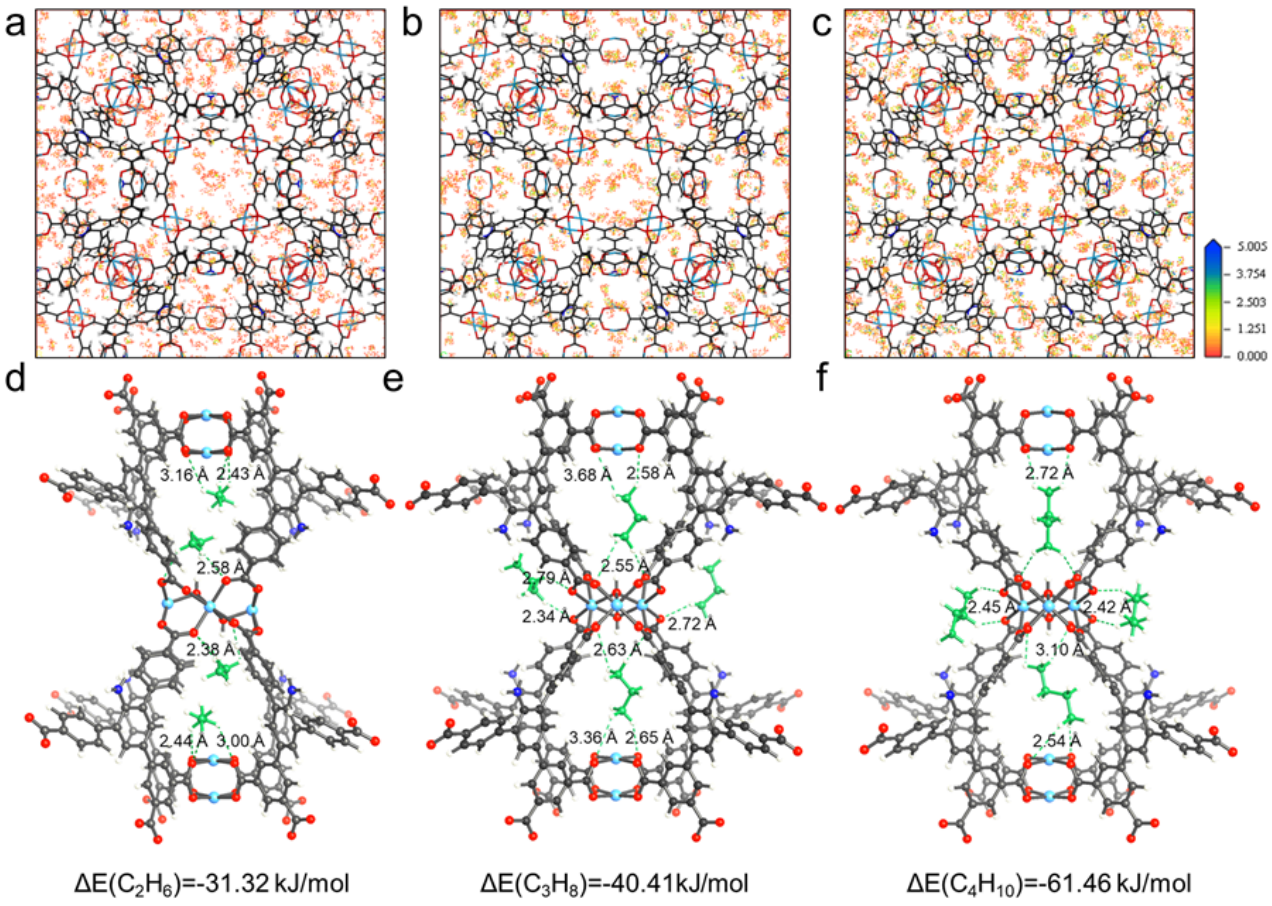


Figure 5

Theoretical calculation of adsorption behavior in UPC-114. Density distribution of **a** C_2H_6, **b** C_3H_8, and **c** C_4H_{10} in UPC-114 at 298 K and 1 bar. DFT-calculated optimal adsorption site and binding energy of **d** C_2H_6, **e** C_3H_8, and **f** C_4H_{10} in UPC-114. Distances are given in Å.

Supplementary Files

This is a list of supplementary files associated with this preprint. Click to download.

- Fan2026UPC114SI.docx
- Fan2026UPC114.pdf
- Fan2026UPC114.cif